

A MEASUREMENT OF  $Z(\nu\bar{\nu})\gamma$  PRODUCTION AND A  
SEARCH FOR NEW PHYSICS IN MONOPHOTON EVENTS  
USING THE CMS DETECTOR AT THE LHC

*by*

James Joseph Buchanan

A dissertation submitted in partial fulfillment of  
the requirements for the degree of

Doctor of Philosophy

(Physics)

*at the*

UNIVERSITY OF WISCONSIN – MADISON

201X

Defended on T.B.D.

Dissertation approved by the following members of the Final Oral Committee:

Sridhara Dasu · Professor of Physics

Wesley Smith · Emeritus Professor of Physics

Matt Herndon · Professor of Physics

T.B.D. · Professor of Physics

T.B.D. · Professor of T.B.D.

© Copyright James Joseph Buchanan 201X  
All Rights Reserved

## Abstract

This thesis presents several studies of monophoton final states using  $35.9\text{ fb}^{-1}$  of 13 TeV proton-proton collision data collected by the CMS experiment at the LHC in 2016. The standard model  $Z(\nu\bar{\nu})\gamma$  cross section is measured as a function of photon transverse momentum. No significant deviations from standard model predictions are observed. The results are also interpreted in the context of several new physics models. Limits are placed on coupling strengths of anomalous triple gauge couplings between photons and  $Z$  bosons, new particle masses in simplified models of dark matter, the suppression scale of a dark matter effective field theory model, and the graviton mass scale in a model of extra spatial dimensions.

# Contents

Abstract . . . . .	i
<b>1 Introduction</b>	<b>1</b>
1.1 Overview . . . . .	1
1.2 Standard model of particle physics . . . . .	2
1.3 $Z(\nu\bar{\nu})\gamma$ cross section . . . . .	7
1.3.1 Previous measurements . . . . .	10
1.4 Anomalous triple gauge couplings . . . . .	11
1.4.1 Previous searches . . . . .	13
1.5 Dark matter EFT and simplified models . . . . .	17
1.5.1 Previous searches . . . . .	21
1.6 ADD gravitons . . . . .	25
1.6.1 Previous searches . . . . .	26
<b>2 The CMS experiment and the LHC</b>	<b>30</b>
2.1 The LHC . . . . .	30
2.1.1 Proton acceleration . . . . .	31
2.1.2 Magnets and beam halo . . . . .	32
2.2 The CMS experiment . . . . .	33
2.2.1 Coordinate system . . . . .	33

2.2.2	Superconducting solenoid and silicon tracking system . . . . .	33
2.2.3	Electromagnetic calorimeter . . . . .	33
2.2.4	Hadronic calorimeter . . . . .	33
2.2.5	Muon systems . . . . .	33
2.2.6	Trigger system . . . . .	33
2.2.7	Luminosity measurement . . . . .	33
<b>3</b>	<b>Simulation</b>	<b>34</b>
3.1	Hard process generation . . . . .	34
3.2	Parton distribution functions . . . . .	34
3.3	Parton showering and hadronization . . . . .	34
3.4	Pileup simulation . . . . .	34
3.5	Detector simulation . . . . .	34
<b>4</b>	<b>Object reconstruction and selection</b>	<b>35</b>
4.1	The particle-flow algorithm . . . . .	35
4.2	Photons and electrons . . . . .	35
4.3	Muons . . . . .	35
4.4	Jets and missing transverse momentum . . . . .	35
4.5	Primary vertex . . . . .	35
<b>5</b>	<b>Event selection</b>	<b>36</b>
5.1	The monophoton signature and background sources . . . . .	36
5.2	Trigger and $p_{\text{T}}^{\text{miss}}$ filters . . . . .	36
5.3	Photon . . . . .	36
5.4	Missing transverse momentum . . . . .	37
5.5	Lepton vetoes . . . . .	37

5.6	Single electron control region . . . . .	37
5.7	Single muon control region . . . . .	37
5.8	Dielectron control region . . . . .	37
5.9	Dimuon control region . . . . .	37
<b>6</b>	<b>Background estimation</b>	<b>38</b>
6.1	Simulated backgrounds . . . . .	38
6.2	Electron faking photon . . . . .	38
6.3	Jet faking photon . . . . .	38
6.4	Spikes . . . . .	38
6.5	Beam halo . . . . .	38
6.6	Transfer factors . . . . .	38
6.7	Likelihood function . . . . .	38
<b>7</b>	<b>Results</b>	<b>39</b>
7.1	$Z(\nu\bar{\nu})\gamma$ cross section . . . . .	39
7.2	aTGC limits . . . . .	39
7.3	DM simplified model limits . . . . .	39
7.4	ADD limits . . . . .	39
<b>8</b>	<b>Conclusions</b>	<b>40</b>
8.1	Summary . . . . .	40
8.2	Outlook . . . . .	40
	<b>Bibliography</b>	<b>41</b>

# Chapter 1

## Introduction

### 1.1 Overview

This thesis presents several analyses of event yields in “monophoton” final states, characterized by a single  $\gamma$  with high transverse momentum, along with an overall transverse momentum imbalance typically of equal magnitude and opposite direction to that of the photon. These analyses correspond to  $35.9 \text{ fb}^{-1}$  of 13 TeV proton-proton ( $pp$ ) collision data collected in 2016 by the CMS detector at the LHC. A measurement of the production rate for the process  $pp \rightarrow Z\gamma \rightarrow \nu\bar{\nu}\gamma$  is obtained and compared to predictions derived from the standard model (SM) of particle physics. No significant deviation from SM predictions is observed.

The predicted monophoton yield in several theories of physics beyond the SM (BSM) is higher than the SM prediction. This thesis examines two varieties of anomalous triple gauge coupling (aTGC), simplified models of dark matter (DM) interacting with SM matter via a vector or axial-vector mediator, an effective field theory (EFT) of DM interaction with  $\gamma$  and  $Z$  bosons, and a model of extra spatial dimensions. For each of these models, 95% confidence level (CL) limits are placed on relevant

parameters based on the observed collision data.

## 1.2 Standard model of particle physics

The “standard model” of particle physics is our current best mathematical framework for describing the behavior of elementary particles. The set of particles described by the SM is illustrated in Fig. 1.1, which groups them according to certain fundamental characteristics. Each particle has an intrinsic angular momentum known as spin, specified by the lower number in each square of Fig. 1.1. Spin can be an integer or half-integer, according to which the particle is classified as a boson or fermion, respectively. The fundamental fermions comprise six “flavors” of quarks ( $u, d, c, s, t, b$ ) and six flavors of leptons ( $e, \mu, \tau$ , along with three corresponding neutrinos  $\nu_e, \nu_\mu, \nu_\tau$ ), each of which has both a particle and an anti-particle variety; the quarks additionally come in three “colors”. We denote a particle by a letter, e.g.  $q$  for a generic quark; its antiparticle partner has an overbar, e.g.  $\bar{q}$ . The fundamental bosons comprise the  $H$  as well as the gauge bosons, in turn comprising the  $Z$ , photon ( $\gamma$ ), two  $W$ s distinguished by their electric charge, and eight gluons ( $g$ ) distinguished by a color-anticolor doublet.

The particles are related to one another through various classes of interactions, each of which has a corresponding charge whose sum must be conserved in any physical process. The electromagnetic and weak interactions correspond to electric charge and weak isospin, respectively. In Fig. 1.1, the value  $Q$  of the electric charge is specified by the middle number in each square. For quarks and leptons, weak isospin determines whether the particle is “up-type” ( $u, d, t, \nu_e, \nu_\mu, \nu_\tau$ ) or “down-type” ( $d, s, b, e, \mu, \tau$ ). Weak isospin has a corresponding value  $T_3$ : up-type fermions have  $T_3 = +1/2$ , down-type fermions and the  $H$  have  $T_3 = -1/2$ ,  $W^\pm$  have  $T_3 = \pm 1$ , and



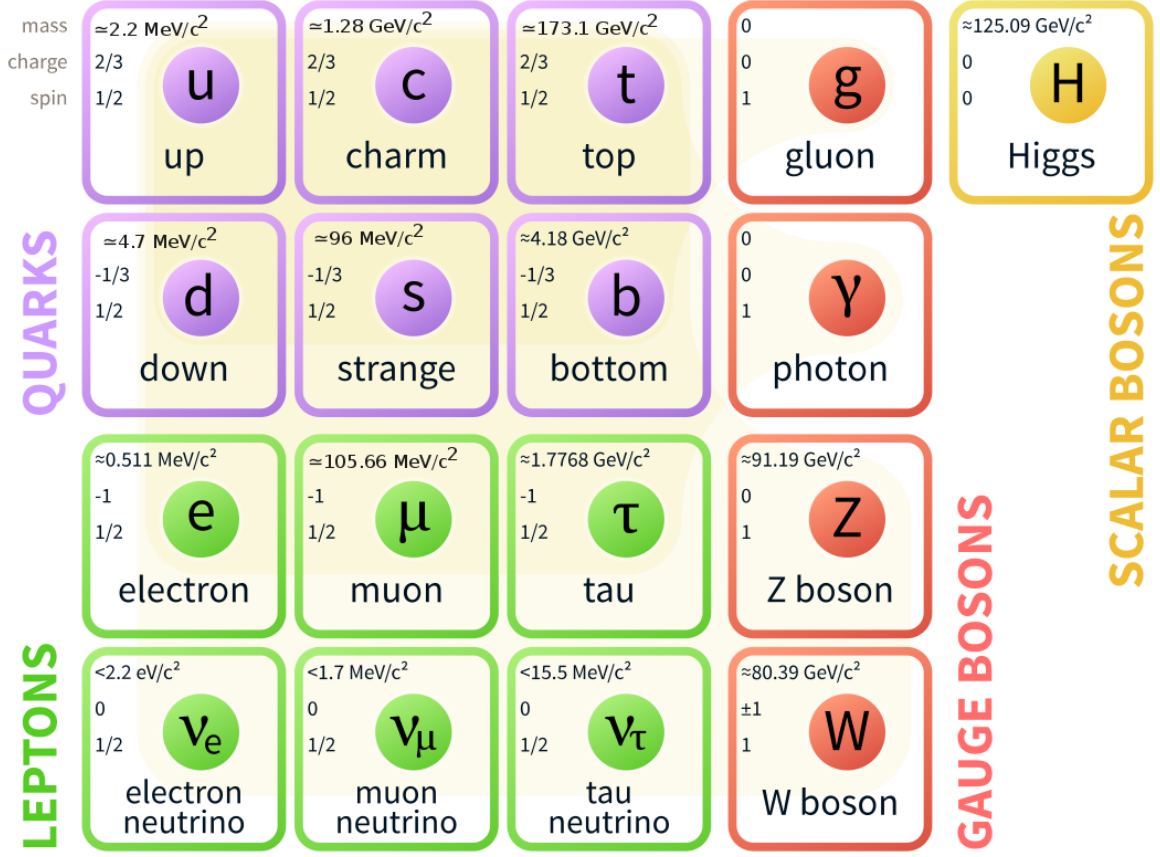


Figure 1.1: The particles of the Standard Model.

the other bosons have  $T_3 = 0$ . The three colors carried by quarks and gluons are associated with a third interaction, described by the theory of quantum chromodynamics (QCD). The preceding discussion applies to normal (i.e. not anti-) particles; antiparticles carry opposite values of all the aforementioned charges.

These interactions lead to the relationships illustrated in Fig. 1.2, in which every linkage represents a direct “coupling”, which allows a particle at one end of the link to evolve directly into a particle at the other end. Particles with a nonzero electric charge are all coupled directly to the photon. The photon is coupled to the weak bosons ( $Z$  and  $W$ ), which in turn couple to all of the fundamental fermions. The gluons couple directly with each other and with the quarks. Particles that couple

directly to the  $H$  have an intrinsic mass (specified by the top number in each square of Fig. 1.1) tied to the strength of their coupling. In the SM, any particle that does not couple directly to the  $H$  is massless.

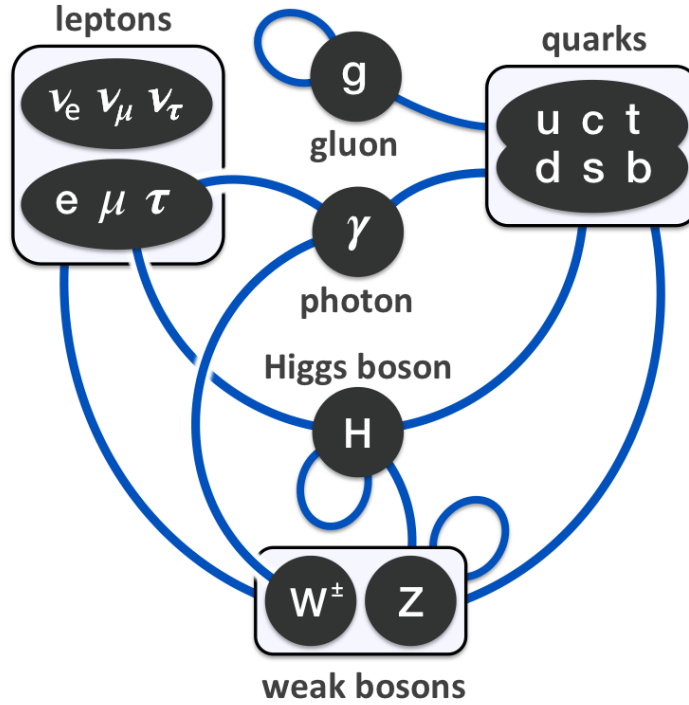


Figure 1.2: Standard Model couplings.

The full dynamics of the SM is encapsulated mathematically by a Lagrangian function. Particles correspond to operator terms appearing in the Lagrangian, and a coupling of one particle to another is described by multiplying their corresponding operators together. The SM Lagrangian is unchanged if all its fermion operators are multiplied by any complex number of the form  $e^{iY\theta}$ , where  $Y$  is a value that depends on the operator being multiplied. This is true even if  $\theta$  is allowed to have different arbitrary values at different points in space and time, but any operator with a nonzero  $Y$  couples to the  $B$ , and as a consequence the first derivatives of  $\theta$  in space and time

must also be subtracted from  $B$ . This deep level of invariance is called a gauge symmetry, with  $B$  the associated gauge boson. Multiplication by  $e^{i\theta}$  is characterized by the group  $U(1)$ , so we say that the SM Lagrangian has a  $U(1)_Y$  gauge symmetry associated with the  $B$ .

In a similar vein, the SM Lagrangian is unchanged if matching doublets of weak isospin up- and down-type operators are multiplied by unitary  $2 \times 2$  matrices with determinant 1, described by the group  $SU(2)$ . Those with a nonzero weak isospin couple to every  $W^i$  ( $i = 1, 2, 3$ ), which must receive their own balancing transformations if the fermion  $SU(2)$  transformations are allowed to vary as a function of space and time. Hence we say that the SM Lagrangian has an  $SU(2)$  gauge symmetry associated with the gauge bosons  $W^i$ .

The  $B$  and  $W^i$ s also couple to the  $H$ , and the structure of this coupling constrains the physical states most easily accessed by these operators, corresponding to four distinct linear combinations of  $B$  and  $W^i$ . These combinations, which are themselves operators, are labeled  $Z$ ,  $\gamma$ ,  $W^+$ , and  $W^-$ , and these are the operators describing the physical particles detected in experiments. In this manner, the electromagnetic and weak interactions are intertwined in what is known as the electroweak (EWK) interaction. The conserved electric charge  $Q$  emerges as the sum of  $T_3$  with  $\frac{1}{2}Y$ .

Finally, the SM Lagrangian has an additional  $SU(3)$  gauge symmetry associated with the eight gluons and color charge, described by QCD. Particles with color charge do not exist stably on their own, but rather are always observed in bound states called hadrons, in which the total color charge of the bound state is invariant under any  $SU(3)$  transformation. One such “colorless” configuration is the proton (p), which to a first approximation may be thought of as a bound state of two  $u$  quarks and one  $d$  quark. However, the mass of the proton is much greater than the sum of the masses of these three components, and this additional mass is associated with an

effervescent “sea” of partons, transient particles swarming the proton that can only be distinguished at high energies. Known partons include all types of quark and antiquark (as well as gluons and photons). As a consequence, a high-energy collision between two protons can give rise to a  $q\bar{q}$  interaction, the primary catalyst for all the processes studied below. A single parton carries some fraction of the total energy carried by the whole proton, so in general, partons collide with a lower interaction energy than that of the protons that carry them. The square of the center-of-mass energy of colliding protons is denoted by  $s$ , while that of a specific parton-parton interaction is denoted by  $\hat{s}$ .

This rapid overview of the SM necessarily elides many essential nuances of the underlying mathematical formalism. These are more fully documented in numerous comprehensive texts on the subject, e.g. [1–5].

The domain of applicability of the SM is quite substantial, encompassing every well-measured fundamental interaction of every verified fundamental particle. All SM particles have been conclusively observed, and no fundamental particles outside the SM have ever been conclusively observed. After decades of effort by thousands of researchers, no significant deviation from SM predictions has ever been confirmed in high-energy scattering experiments [6]. These efforts are extended here with studies of the relationship between  $Z$  and  $\gamma$  (sec. 1.3 and 1.4) at state-of-the-art precision. There are nevertheless many physical phenomena that the SM does not account for. The analyses presented here investigate the nature of gravitation (sec. 1.6), including the gravitational phenomenon known as DM (sec. 1.5), neither of which have an SM description.

### 1.3 $Z(\nu\bar{\nu})\gamma$ cross section

In a collision of two beams of particles, the average rate of any specific collision process is directly proportional to the number of particles in each of the colliding beams, to their density in the plane transverse to the beam direction, and to the average frequency at which particles are made to come into contact. These features determine the instantaneous luminosity  $L$  of a pair of colliding beams, and the overall average rate of a given process may be written as  $\sigma L$ , where  $\sigma$  is a constant of proportionality. Since  $\sigma$  has dimensions of area, it is called the cross section.

Cross sections may be calculated using Feynman diagrams. These are assembled by combining fundamental interaction vertices: the SM vertices relating the fermions and gauge bosons are listed in Fig. 1.3. Mathematical terms are assigned to Feynman diagrams according to a prescription known as the Feynman rules, which can be derived from the Lagrangian. This process results in a mathematical expression  $\mathcal{M}_i$  for each diagram  $i$  one wishes to consider. The cross section is proportional to the sum of  $|\sum_i \mathcal{M}_i|^2 \rho$  over all kinematically consistent initial and final states of the given process<sup>1</sup>. This method for calculating cross sections using Feynman diagrams is more fully described in refs. [1,2]; a development in the context of quantum field theory is given in e.g. refs. [3–5].

The Feynman rule for a vertex includes a numerical factor  $g$ . These are typically less than 1 in high-energy collisions, and therefore diagrams with additional vertices make smaller contributions to a cross section calculation. The expression  $|\sum_i \mathcal{M}_i|^2$  can therefore be organized as a sum of terms with increasing powers of  $\alpha \propto g^2$ , which make successively smaller contributions to the cross section. Terms with the lowest powers of  $\alpha$  are called leading order (LO) terms, followed by next-to-leading order (NLO), next-to-next-to-leading order (NNLO), etc. Diagrams with an internal

---

<sup>1</sup> $\rho$  is a function of the allowed kinematic parameters and is called the phase space factor

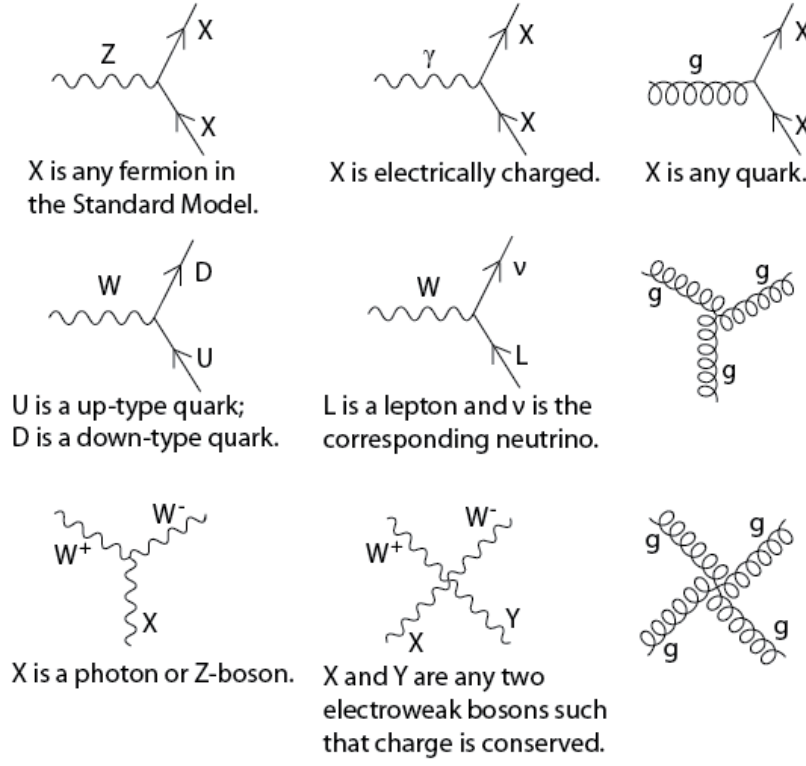


Figure 1.3: Fermion and gauge boson vertices of the standard model.

loop contain at least one more vertex than equivalent diagrams without the loop, and therefore diagrams without any internal loops, called tree-level diagrams, make the only contributions at LO (when they exist). Each class of interaction has its own characteristic  $\alpha$ : an undecorated  $\alpha$  usually refers to the fine structure constant characterizing electromagnetic processes, while QCD is characterized by  $\alpha_s$ .

In the SM, events with a monophoton signature arise at the LHC (Chap. 2) primarily from the process  $q\bar{q} \rightarrow Z\gamma \rightarrow \nu\bar{\nu}\gamma$ , where  $q$  is any single species of quark,  $\nu$  is any single species of neutrino, and the neutrino-antineutrino pair arises from the decay of a short-lived  $Z$  boson. The leading tree-level diagram for this process is shown in Fig. 1.4(a). We typically abbreviate this process by reference to its final state,  $Z(\nu\bar{\nu})\gamma$ . The final-state photon can be detected, but the neutrinos only interact

with SM particles via the mediation of  $Z$  and  $W$  bosons, and these interactions are strongly suppressed by the high masses of those particles. Hence, neutrinos almost never interact directly with the LHC's detectors.

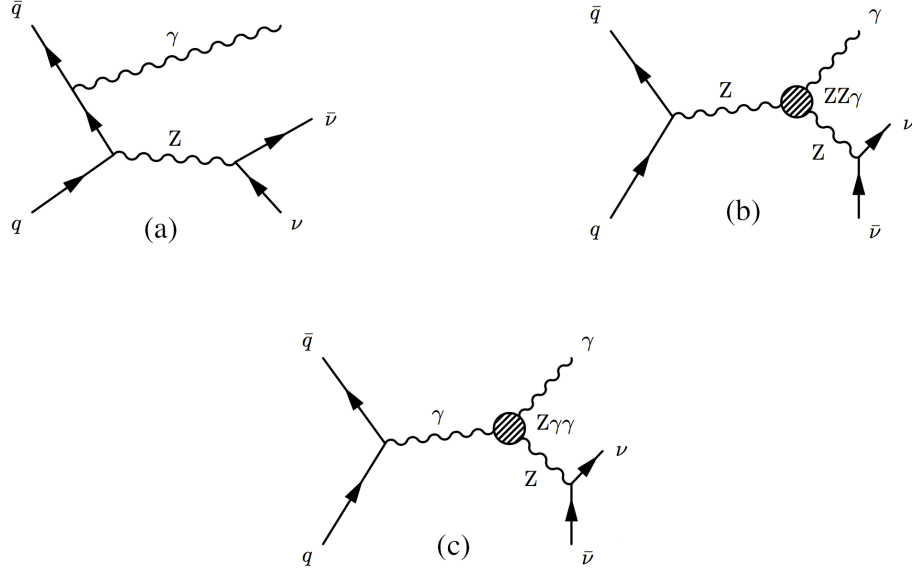


Figure 1.4: The leading Feynman diagrams for  $Z(\nu\bar{\nu})\gamma$  production arising from  $pp$  collisions. Diagram (a) is the leading SM contribution. Diagrams (b) and (c) show contributions from aTGC vertices.

Their existence is instead inferred by their absence. In a collider experiment, the vectorial momentum transverse to the beam direction,  $\vec{p}_T$ , must sum to approximately zero in the reference frame of the detector. The negative vector sum of  $\vec{p}_T$  for all detected particles in an event is denoted  $\vec{p}_T^{\text{miss}}$ , and its magnitude  $p_T^{\text{miss}}$  must therefore be close to zero if all the particles in an event are reliably detected and their momenta are accurately measured. The only high-momentum SM particles that can't be reliably detected are neutrinos, so a large value of  $p_T^{\text{miss}}$  can be a sign of neutrino production. An event with a high- $p_T$  detected photon, in which the  $\vec{p}_T^{\text{miss}}$  has a large magnitude and points in a direction significantly different from that of the photon,

is called a monophoton event, and it is expected that  $Z(\nu\bar{\nu})\gamma$  processes are the main contributors of high- $p_T$  monophoton events.

The theoretical SM value for the  $Z(\nu\bar{\nu})\gamma$  cross section has been calculated to NLO in  $\alpha$  and  $\alpha_S$  [7,8]. Events with additional radiated photons, quarks, or gluons are also included at this order. The  $Z(\nu\bar{\nu})\gamma$  process receives NLO contributions from 1-loop QCD and EWK diagrams, as well as tree-level diagrams with up to one additional radiated  $\gamma$ ,  $q$ , or  $g$ . These can arise from initial-state  $q\bar{q}$ ,  $qg$ , and  $\bar{q}g$  (with QCD and EWK corrections at NLO), as well as  $q\gamma$ ,  $\bar{q}\gamma$  (with EWK corrections at NLO) [8].

The calculation has also been done to NNLO in  $\alpha_S$  alone, which includes contributions from tree-level diagrams with up to two extra radiated QCD partons ( $q$  or  $g$ ), one-loop diagrams with up to one extra radiated QCD parton, and two-loop corrections. The initial-state QCD parton interactions include those listed among the NLO contributions above, as well as  $gg$  [9,10].

The exact values obtained from any such calculation depend on the specific initial and final states included. These restrictions (cuts) on events are informed by the operating conditions of the experiment one wishes to compare results with.

### 1.3.1 Previous measurements

Experiments at the LEP detector measured the cross section of  $Z(\nu\bar{\nu})\gamma$  arising from  $e^+e^-$  collisions for  $\sqrt{s}$  up to  $\sim 200$  GeV. The L3 experiment measured the cross section to be  $5.1 \pm 0.3(\text{stat}) \pm 0.1(\text{syst})$  pb based on  $175.6$  pb $^{-1}$  of collision data with an average  $\sqrt{s} = 188.6$  GeV, compared to an SM prediction of  $4.99 \pm 0.05(\text{stat})$  [11]. Looking at collision data at the same  $\sqrt{s}$ , but with different cuts, the OPAL experiment measured the cross section to be  $2.52 \pm 0.13(\text{stat}) \pm 0.05(\text{syst})$  pb based on  $177.3$  pb $^{-1}$  of data, compared to an SM prediction of  $2.81 \pm 0.02(\text{stat})$  pb. This set of SM predictions were made up to  $O(\alpha^2)$ , but LO in  $\alpha_S$ .



The D0 experiment at the Tevatron made the first observation of  $Z(\nu\bar{\nu})\gamma$  arising from  $p\bar{p}$  collisions in 2009. This yielded a cross section measurement of  $32 \pm 9(\text{stat} + \text{syst}) \pm 2(\text{lumi}) \text{ fb}$  for a leading photon  $p_T$  above 90 GeV, compared to an SM prediction of  $39 \pm 4(\text{theory}) \text{ fb}$  computed to NLO in  $\alpha_S$  [12].

Measurements of the cross section at higher values of  $p_T^\gamma$  have been performed by experiments examining  $pp$  collision data at the LHC. An analysis by the CMS experiment examining  $19.6 \text{ fb}^{-1}$  of data collected at  $\sqrt{s} = 8 \text{ TeV}$  found the observed  $Z(\nu\bar{\nu})\gamma$  cross section for  $p_T^\gamma > 145 \text{ GeV}$  to be  $52.7 \pm 2.1(\text{stat}) \pm 6.4(\text{syst}) \pm 1.4(\text{lumi}) \text{ fb}$ , compared to an SM prediction of  $40.7 \pm 4.9(\text{theory}) \text{ fb}$  calculated to NLO in  $\alpha_S$  and a prediction of  $50.0_{-2.2}^{+2.4}(\text{theory})$  calculated to NNLO in  $\alpha_S$  [13]. This comparison illustrates the need for NNLO precision at high  $p_T^\gamma$ .

The most precise measurement of the  $Z(\nu\bar{\nu})\gamma$  cross section for  $p_T^\gamma$  and  $p_T^{\text{miss}}$  above 150 GeV currently comes from an analysis of  $36.1 \text{ fb}^{-1}$  of  $pp$  collision data collected by the ATLAS experiment at  $\sqrt{s} = 13 \text{ TeV}$ , with an observed cross section of  $83.7_{-3.5}^{+3.6}(\text{stat})_{-6.2}^{+6.9}(\text{syst})_{-2.0}^{+1.7}(\text{lumi}) \text{ fb}$ . The corresponding SM prediction, computed to NNLO in  $\alpha_S$  using the MATRIX generator [14], is  $78.6 \pm 0.4(\text{stat}) \pm 4.1(\text{syst}) \text{ fb}$  [15]. The cross section is shown in discrete ranges (bins) of leading photon  $p_T$  in Fig. 1.5.

None of these analyses report any significant deviation from SM predictions.

## 1.4 Anomalous triple gauge couplings

Putative vertices joining three particles that are not found in the SM are known as aTGCs. For example, there is no fundamental SM vertex joining a single  $\gamma$  to a pair of  $Z$ s, or a single  $Z$  to a pair of  $\gamma$ s. A model describing the generic phenomenology of these aTGCs is developed in [18–20]. For an intermediate state  $V = Z, \gamma$  decaying to a final state  $Z\gamma$  pair, this model parametrizes the effective vertex interaction  $ZV\gamma$

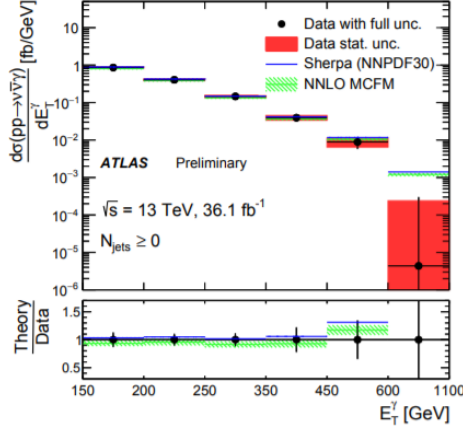


Figure 1.5: Cross section of  $Z(\nu\bar{\nu})\gamma$  production plotted in bins of leading photon  $p_T$  ( $E_T^\gamma$ ), as shown in [15]. The blue and green bands show the SM predictions derived from the Sherpa [16] and MCFM [17] generators, respectively.

by a set of factors  $h_i^V$  ( $i$  from 1 to 4). Increasing the values of these parameters significantly increases the cross section of  $Z(\nu\bar{\nu})\gamma$  processes, by allowing the reaction to proceed via the additional diagrams shown in Fig. 1.4(b),(c), in which the aTGC vertices are covered by opaque circles.

The circle could be thought of as masking a more detailed process taking place underneath. The SM admits processes that are predicted to contribute to this effective vertex, but all SM contributions to  $h_{3,4}^V$  have at least one internal loop that could fit within the circle, and further loops are required for  $h_{1,2}^V$  contributions [19]. As a consequence, the SM contribution to all eight  $h_i^V$  parameters is quite close to zero. The observation of a substantial nonzero value for any  $h_i^V$  would be a compelling sign of BSM physics.

The contributions to the  $Z(\nu\bar{\nu})\gamma$  cross section coming from  $h_{1,2}^V$  are independent of those from  $h_{3,4}^V$  (for any  $V$ ), and also nearly identical in magnitude, so without loss of generality we only focus on scenarios for which  $h_{3,4}^V$  are nonzero. The contributions from  $h_i^Z$  are largely independent of those from  $h_j^\gamma$  (for any  $i,j$ ), so these are examined

separately. However, the contributions from  $h_3^V$  are substantially correlated with those from  $h_4^V$  (and similarly for  $h_{1,2}^V$ ), so we examine scenarios in which  $h_{3,4}^V$  take on assorted pairs of values, both of which may be nonzero. The theoretical relationships between these parameters are explored in [19].

The neutrino decays of  $Z$ -bosons offer an especially good window on  $ZZ\gamma$  and  $Z\gamma\gamma$  aTGCs because the probability of  $Z$  decays into neutrinos is roughly six times higher than that of decays into  $e^+e^-$ , and also into  $\mu^+\mu^-$ . Furthermore, the probability of reconstructing a  $Z(\nu\bar{\nu})\gamma$  event in a detector is typically higher than that of a charged lepton event. As a consequence, aTGC limits derived from neutral  $Z$  decays can be several times finer than limits derived from charged  $Z$  decays when analyzing the same  $pp$  collision data sets (compare e.g. [21] and [22], based on 7 TeV LHC data; also Fig. 1.8, based on 8 TeV data). The decays of  $Z$  into  $q\bar{q}$  (and thence to hadrons) are difficult to distinguish in practice from hadronic  $W$  decays [23].

### 1.4.1 Previous searches

The LEP collider established constraints on each of the eight the parameters  $h_i^V$  in the context of the process  $e^+e^- \rightarrow Z\gamma$ . In a statistical combination of searches performed by the DELPHI, L3, and OPAL experiments, examining  $3\text{ fb}^{-1}$  of  $e^+e^-$  collision data for  $\sqrt{s}$  ranging from 130 GeV to 209 GeV, the 95% CL intervals of seven of the parameters contain 0, with total ranges between 0.05 and 0.10 for  $h_i^\gamma$  and between 0.14 and 0.25 for  $h_i^Z$ ; the 95% CL interval for the remaining factor  $h_4^\gamma$  spans 0.01 to 0.05 [24].

The LEP combined analysis assumed that all but one of the eight parameters were fixed to the SM expectation of 0 (i.e. these are 1D limits). It was also the last major effort to obtain limits on  $h_{1,2}^V$  independently of  $h_{3,4}^V$ , as subsequent searches have taken the present approach of focusing on  $h_{3,4}^V$  alone, for the reasons listed above. Uniquely

among the LEP experiments, the L3 Collaboration also placed limits on correlated pairs of parameters (2D limits), shown in Fig. 1.6 [11].

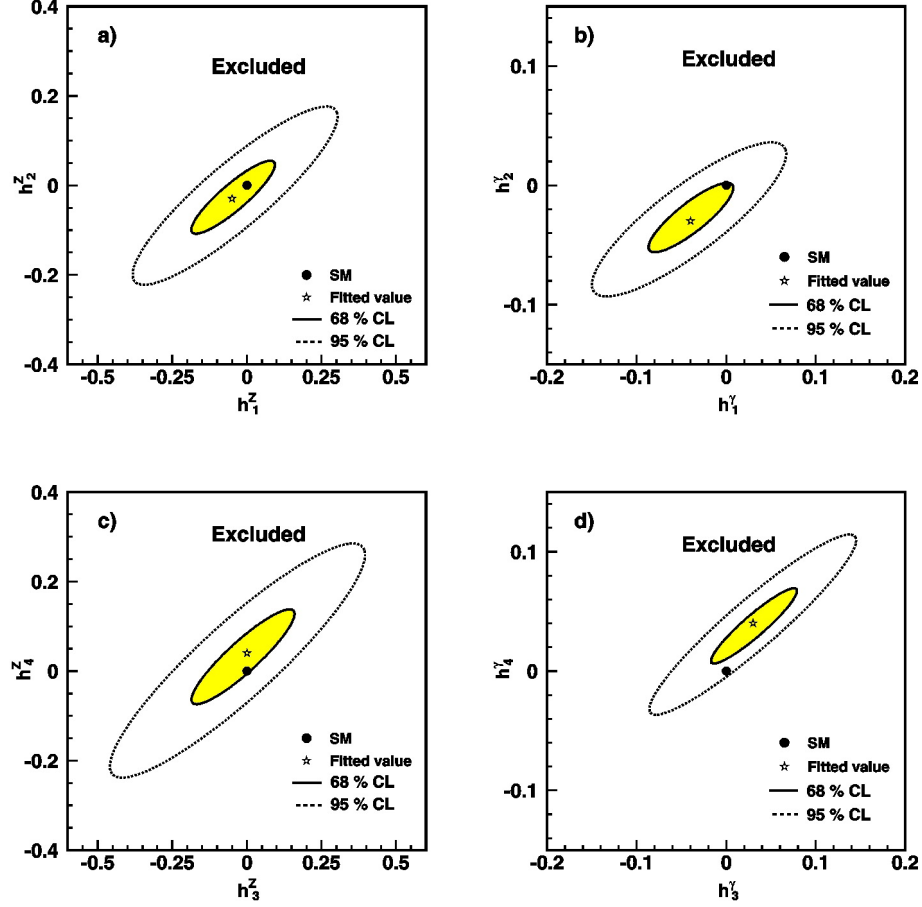


Figure 1.6:  $h_i^V$  exclusion contours from the L3 experiment at the LEP collider, as shown in [11].

Experiments at the Tevatron collider improved these limits in analyses of  $p\bar{p}$  collision data at  $\sqrt{s} = 1.96$  TeV. The Tevatron analyses incorporated a form factor  $1/(1 + \hat{s}/\Lambda^2)^n$ , by which a constant term  $h_{0i}^V$  is multiplied to obtain  $h_i^V$ . The form factor is essentially arbitrary;  $n$  is set equal to  $i$  and  $\Lambda$  (not to be confused with the EFT suppression scale, below) is set to 1.5 TeV by convention. This form factor was introduced in the common reference [19] but was not used in LEP [24] or most

subsequent LHC analyses, which treat the  $h_i^V$  parameters as constants independent of  $\hat{s}$ .

The CDF experiment combined analyses of  $Z(\nu\bar{\nu})\gamma$  processes, using  $4.9 \text{ fb}^{-1}$  of data, and processes where the  $Z$  decays to  $e^+e^-$  or  $\mu^+\mu^-$ , using  $5.1 \text{ fb}^{-1}$  of data. They set 95% Bayesian credibility intervals constraining  $|h_3^V| < 0.022$  and  $|h_4^V| < 0.0009$  (1D limits) [25]. The D0 experiment similarly combined a  $3.6 \text{ fb}^{-1}$   $Z(\nu\bar{\nu})\gamma$  analysis with a  $7.2 \text{ fb}^{-1}$   $Z(e^+e^-)\gamma$  and  $Z(\mu^+\mu^-)\gamma$  analysis to set 95% CL limits constraining  $|h_{03}^V| < 0.027$  and  $|h_{04}^V| < 0.0014$  (1D limits) [26]. Correlated 2D limits were also computed and are shown in Fig. 1.7.

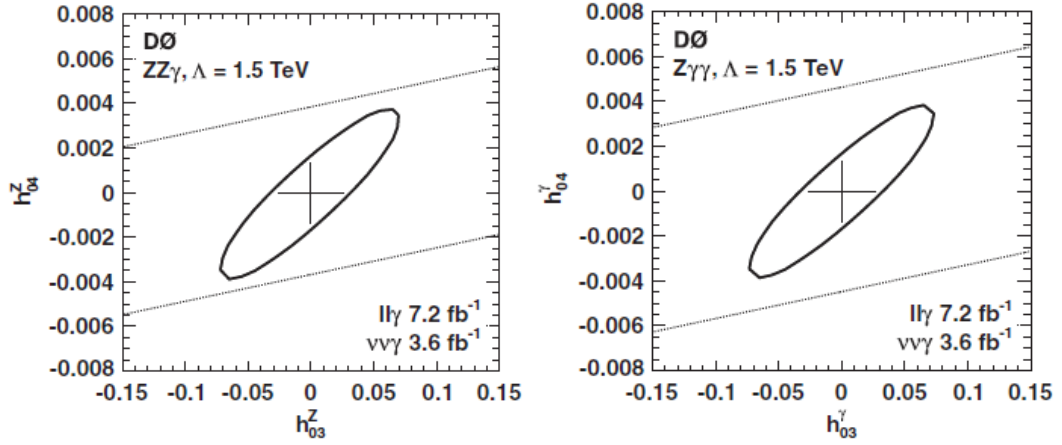


Figure 1.7:  $h_{0i}^V$  exclusion contours from the D0 experiment at the Tevatron collider, as shown in [26].

Experiments at the LHC made further improvements via the analysis of  $pp$  collision data at progressively higher  $\sqrt{s}$ . A summary of 1D limits on  $h_i^V$  from both the ATLAS and CMS experiments obtained from analyses of  $\sim 20 \text{ fb}^{-1}$  of  $\sqrt{s} = 8 \text{ TeV}$  data is shown in Fig. 1.8. ATLAS limits show the results of combined  $Z(\nu\bar{\nu})\gamma$ ,  $Z(e^+e^-)\gamma$ , and  $Z(\mu^+\mu^-)\gamma$  analyses, both with and without a form factor on  $h_i^V$ . CMS limits show separate  $Z(\nu\bar{\nu})\gamma$  results, along with combined  $Z(e^+e^-)\gamma$  and  $Z(\mu^+\mu^-)\gamma$

results, both without a form factor [23]. These comparisons make clear that  $Z(\nu\bar{\nu})\gamma$  is by far the more sensitive channel for setting aTGC limits.

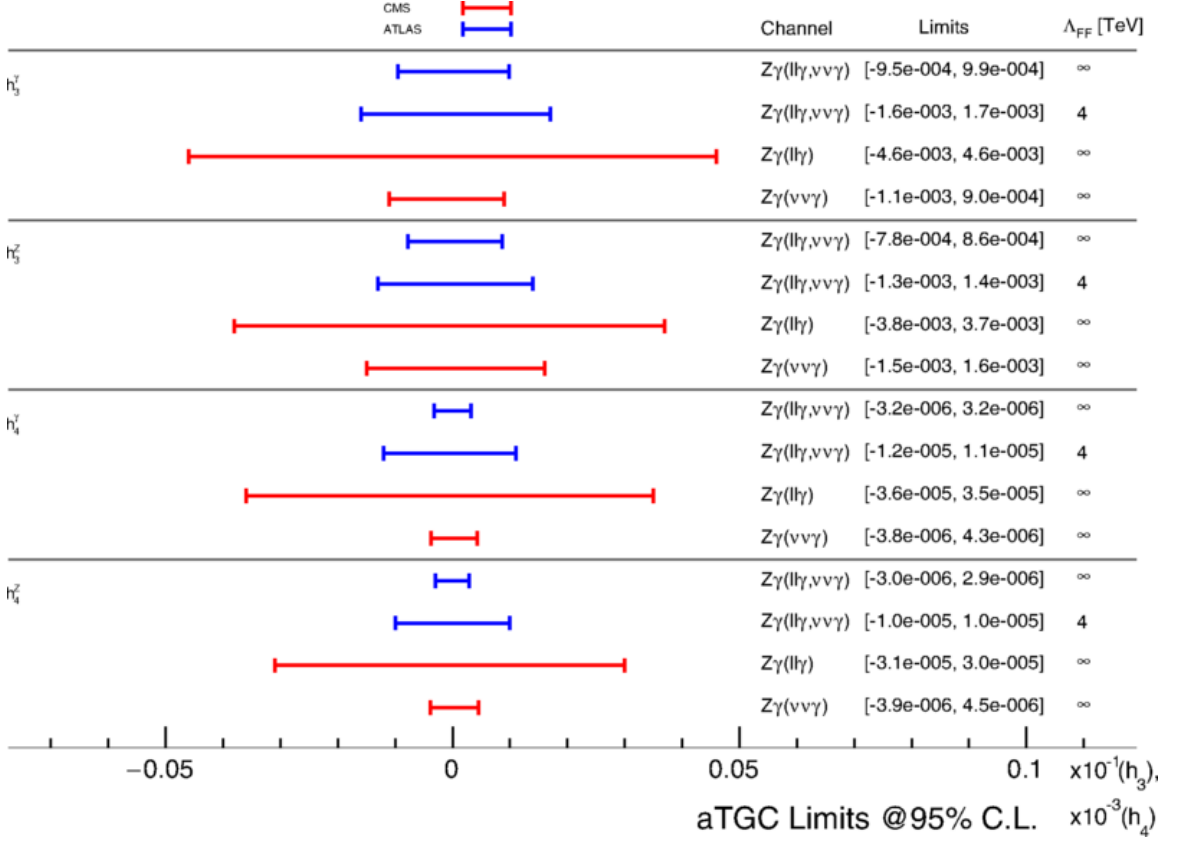


Figure 1.8: 1D  $h_i^V$  exclusion limits from the ATLAS and CMS experiments at the LHC based on  $20\text{ fb}^{-1}$  of  $\sqrt{s} = 8\text{ TeV}$   $pp$  collision data, as shown in [23].  $Z\gamma(l\bar{l}\gamma)$  indicates a combination of  $Z(e^+e^-)\gamma$  and  $Z(\mu^+\mu^-)\gamma$  analyses;  $Z\gamma(l\bar{l}\gamma, \nu\bar{\nu}\gamma)$  indicates a combination of these with  $Z(\nu\bar{\nu})\gamma$ . The mass  $\Lambda_{FF}$  is the form factor scale;  $\infty$  means no form factor was used.

The most sensitive published limits on  $h_{3,4}^{Z,\gamma}$  are currently derived from  $36.1\text{ fb}^{-1}$  of  $13\text{ TeV}$   $pp$  collision data collected by the ATLAS detector at the LHC, analyzed exclusively in the monophoton channel, with no form factor [15]. These are summarized in Figs. 1.9, 1.10.

None of these analyses report any significant evidence of BSM physics.

Parameter	Limit 95% C.L.	
	Measured	Expected
$h_3^\gamma$	$(-3.7 \times 10^{-4}, 3.7 \times 10^{-4})$	$(-4.2 \times 10^{-4}, 4.3 \times 10^{-4})$
$h_3^Z$	$(-3.2 \times 10^{-4}, 3.3 \times 10^{-4})$	$(-3.8 \times 10^{-4}, 3.8 \times 10^{-4})$
$h_4^\gamma$	$(-4.4 \times 10^{-7}, 4.3 \times 10^{-7})$	$(-5.1 \times 10^{-7}, 5.0 \times 10^{-7})$
$h_4^Z$	$(-4.5 \times 10^{-7}, 4.4 \times 10^{-7})$	$(-5.3 \times 10^{-7}, 5.1 \times 10^{-7})$

Figure 1.9: 1D  $h_i^V$  exclusion limits from the ATLAS experiment at the LHC based on  $36.1 \text{ fb}^{-1}$  of  $\sqrt{s} = 13 \text{ TeV}$   $pp$  collision data, analyzed in the monophoton channel, as shown in [15].

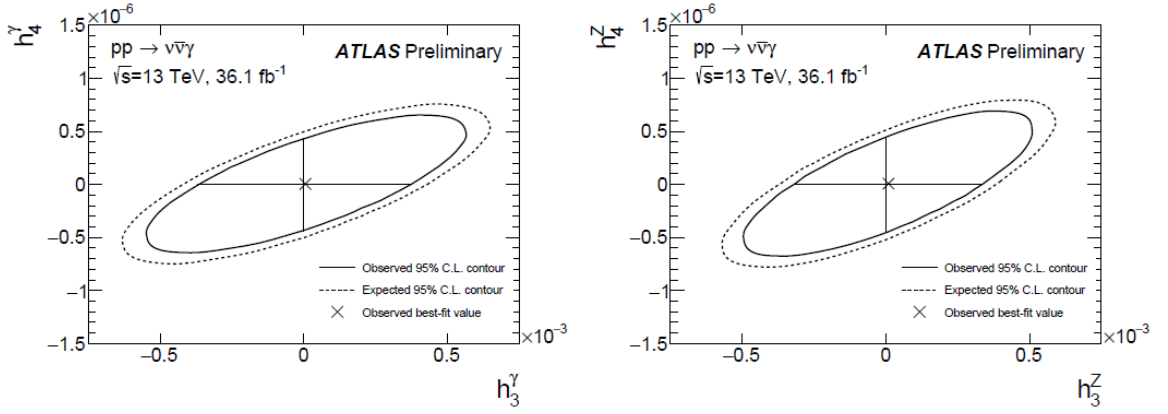


Figure 1.10: 2D  $h_i^V$  exclusion contours from the ATLAS experiment at the LHC based on  $36.1 \text{ fb}^{-1}$  of  $\sqrt{s} = 13 \text{ TeV}$   $pp$  collision data, analyzed in the monophoton channel, as shown in [15].

## 1.5 Dark matter EFT and simplified models

The standard theory of gravitation, Einstein's general theory of relativity (GR), has passed experimental tests over scales ranging from the orbits of satellites [27] to the entire observable universe [28], matching observations more closely than Newton's theory of gravitation, to which it converges in the weak-field limit [29]. It predicts the existence of gravitational waves, directly detected for the first time in 2015 [30],

and these have been used to test the theory in the strong-field regime [31].

Despite its many triumphs, GR plainly fails—under the assumption that SM particles are the only sort that exist—to describe the orbits of stars in nearly every galaxy [32], the average weak distortion of light by galaxies [33], the strong distortion of light by galaxy clusters [34], the orbits of galaxies in galaxy clusters [35], the formation of large-scale filamentary structures [36], or the distribution of ripples in the cosmic microwave background (CMB) arising from big bang nucleosynthesis [28]. Each of these phenomena appear to indicate the existence of an abundance of massive matter with no discernible interactions of any sort other than its gravitational pull. This extends to interactions with visible light, giving rise to the name “dark matter.”

These difficulties could indicate the need to modify the theory of gravity. However, the nature of the Bullet cluster, a galaxy cluster with a center of mass displaced from its visible mass center, is challenging to explain in a theory of gravity without DM that can also explain all of the preceding observations; in contrast, it has a straightforward explanation if GR+DM is true [37]. Furthermore, if a modified theory of gravity produces the apparent gravitational effect of DM on galactic scales, then the existence of a galaxy without any apparent DM, as observed in [32], is also challenging to explain.

No SM particle is predicted to exhibit the behavior of DM, and this has spurred the development of BSM theories describing new particles that could account for it [38–41]. The great diversity of theories motivates general models that can potentially constrain a wide variety of specific theories simultaneously. If DM is particulate in nature, it apparently has a substantial mass, interacts very weakly with SM particles, and is stable on cosmological timescales, and the models we consider include a BSM particle satisfying these criteria. All the massive, stable particles in the SM are fermionic, and these models similarly describe a fermionic DM candidate. Otherwise,



the new physics content of these models is kept to a minimum, as sufficiently large deviations from SM predictions would presumably have been detected by now.

One model we examine describes a direct coupling between DM and the neutral EWK vector bosons  $Z$  and  $\gamma$  [42]. The model does not fully specify the nature of the proposed particle and its SM interactions, but rather only predicts the most dominant potential signature of new physics, by adding a handful of new operator terms to the SM Lagrangian. Any operator has a “mass dimension”, denoted in powers of GeV. The SM Lagrangian has a mass dimension of 4, and any operator term added to it has to have this same mass dimension for the expression to be coherent. Additional particle interactions in an operator term tend to raise the mass dimension. If an operator describes an especially intricate interaction, the overall term must be multiplied by an extra factor of  $(\frac{1}{\Lambda})^n$  to maintain an overall mass dimension of 4, where  $\Lambda$  is some mass scale in GeV and  $n$  is a positive number.

Operator terms with nonzero powers of  $\frac{1}{\Lambda}$  tend to have their interactions suppressed for interaction energies much smaller than  $\Lambda$ , and so  $\Lambda$  is called the suppression scale. The effects of more complicated terms, multiplied by higher powers of  $\frac{1}{\Lambda}$ , are expected to become apparent at higher energy scales, so a model that only incorporates simpler terms is expected to lose predictive validity as  $\Lambda$  is approached [43]. A model that only adds a restricted set of terms, with predictive validity only up to energies below  $\Lambda$ , is called an EFT.

The DM-EWK EFT described in [42] adds four dimension-7 interaction terms to the SM Lagrangian, which therefore carry factors of  $\frac{1}{\Lambda}$  raised to the third power. The mass  $m_{\text{DM}}$  of the new DM particle is a free parameter of the model, along with two constants  $k_1$  and  $k_2$  controlling the relative strengths of the DM- $Z$  and DM- $\gamma$  couplings. Fig. 1.11 illustrates the dominant contribution of this interaction to monophoton yields. Since the DM particle only interacts with the  $Z$  and  $\gamma$ , and this

interaction is suppressed by  $(\frac{1}{\Lambda})^3$ , the outgoing DM is not expected to interact at all with any detector apparatus.

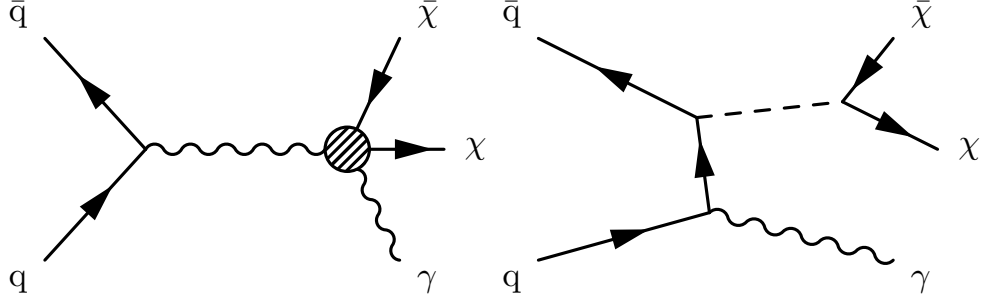


Figure 1.11: Leading order Feynman diagrams for monophoton processes in a DM-EWK EFT (left) and in DM simplified models (right). The intermediate boson in the EFT diagram can be a  $Z$  or  $\gamma$ . The dotted line in the DM simplified model diagram stands for the DM-quark mediator.

Since the DM emerges directly from an EWK boson, this EFT is limited in the sort of dynamics it can describe. So-called simplified models of DM add a new mediating boson between the DM and SM fermions [44], which more typically characterizes the fermion interactions that we know from the SM. We examine models in which the mediator has either exclusively vector or exclusively axial-vector couplings to DM and also to SM quarks, independently of quark flavor. The free parameters of this model include the DM mass  $m_{\text{DM}}$ , the mediator mass  $M_{\text{med}}$ , the DM-mediator coupling  $g_{\text{DM}}$  and the DM-quark coupling  $g_{\text{q}}$ . The leading Feynman diagrams for monophoton production are shown in Fig. 1.11. The mediators are typically chosen to be quite massive, which suppresses the likelihood of DM-quark interactions, and the mediator does not have any direct couplings to leptons or bosons, so the DM is not expected to interact with detector elements as it escapes.

### 1.5.1 Previous searches

In the limit that  $M_{\text{med}}$  is much larger than the  $q\bar{q}$  interaction energy, DM simplified models converge to an EFT describing a direct contact interaction between DM and quarks, with a suppression scale  $M_* = M_{\text{med}}/\sqrt{g_q g_{\text{DM}}}$  [45]. Such DM-quark EFT models were the subject of monophoton searches [46, 47] prior to the adoption of DM simplified models by the ATLAS-CMS Dark Matter Forum in 2015 [44]. As the interaction energy increases, the EFT description breaks down for the reasons described above, and DM simplified models offer a replacement that retains predictive validity (at the cost of some degree of generality). In contrast, the dimension-7 DM-EWK EFT considered here is not the large- $M_{\text{med}}$  limit of a DM simplified model [44] and represents a truly distinct process topology.

Both the DM simplified models and the DM-EWK EFT were developed after LHC data taking began, with comparisons to LHC data in mind [42, 44]. Thus, the history of examination of these models begins with analyses of data collected by the ATLAS and CMS experiments at the LHC. In general, limits on BSM models set by LHC experiments become stronger at higher energies and with larger data sets. The remainder of this section describes the most stringent experimental limits set by the ATLAS and CMS experiments, each based on analyses of 13 TeV  $pp$  collision data collected in 2016.

New physics introduced by DM simplified models is expected to contribute to a variety of other signatures in addition to the monophoton signature. Figure 1.12 compares analyses in three different “mono-X” channels based on data collected by the CMS detector, including the most recent monophoton results described herein. Each of the three searches examine similar final state characteristics; they are primarily distinguished by the type of particle(s) emerging against the  $\vec{p}_{\text{T}}^{\text{miss}}$ , listed in the caption. The limits on DM simplified model parameters set by the monophoton

search are generally more stringent than those set by mono- $Z$  search, but less stringent than those set by the mono- $j/V$  search. The concordance of results from each of these three independent analyses reinforces the degree of confidence with which model parameters are excluded, and in the event of a new physics discovery in one channel, the nature of the discovery will be further illuminated by searching for a corroborating signature in other channels.

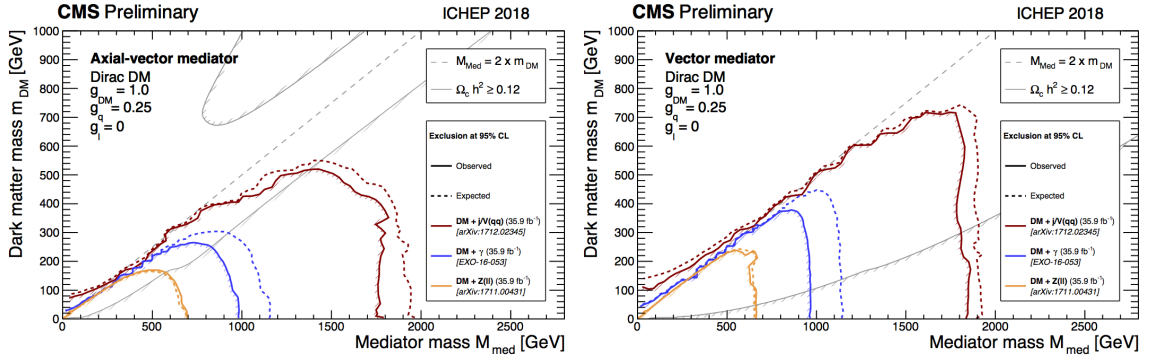


Figure 1.12: Summary plots of limits on DM simplified model parameters, shown in [48]. Simplified models are excluded at 95% CL or above for parameter values under the contours. Results based on three different final states are shown: mono- $Z(l\bar{l})$  [49] in yellow, mono- $j/V(q\bar{q})$  [50] in red, and monophoton [51] in blue, the latter corresponding to the new results presented in this thesis. The  $\Omega_c^2$  curves correspond to constraints on the cosmological DM abundance set by Planck satellite measurements [28].

Prior to the present analysis, the last published results from CMS in the monophoton final state examined  $12.9 \text{ fb}^{-1}$  of data collected in the first half of 2016 [52]. Simplified models were excluded at 95% CL for  $M_{\text{med}}$  up to 700 GeV at small values of  $m_{\text{DM}}$ , in both the vector and axial-vector cases. Values of  $\Lambda$  for the DM-EWK EFT up to 600 GeV were also excluded at 95% CL, assuming  $k_1 = k_2 = 1^2$ .

<sup>2</sup>Defining  $k = \sqrt{k_1^2 + k_2^2}$  and  $\theta_k = \arctan \frac{k_2}{k_1}$ , the choice  $k_1 = k_2 = 1$  corresponds to the choice  $k = \sqrt{2}$  and  $\theta_k = \pi/4$ . Fixing  $\theta_k = \pi/4$ , the limits on  $\Lambda/k^{1/3}$  for arbitrary  $k$  are equal to the  $k = \sqrt{2}$  limits on  $\Lambda$  multiplied by  $2^{-1/6}$ .

The most stringent monophoton results to date are set by an analysis of  $36.1 \text{ fb}^{-1}$  of data collected by the ATLAS detector [53]. Simplified models were excluded at 95% CL for  $M_{\text{med}}$  up to 1200 GeV at small values of  $m_{\text{DM}}$ , in both the vector and axial-vector cases, as shown in Fig. 1.13. Values of  $\Lambda$  for the DM-EWK EFT up to 790 GeV, assuming  $k_1 = k_2 = 1$ , were also excluded at 95% CL, as shown in Fig. 1.14.

Assuming DM simplified models describe the dominant mode of interaction between DM and SM particles, the scattering cross section of low-energy (nonrelativistic) DM off nucleons (protons and neutrons) is uniquely determined [45]. This allows DM simplified model limits to be compared directly with limits set by direct detection (DD) experiments, which search for freely-floating ambient DM by looking for signatures of DM scattering off of target nuclei. The most recent ATLAS results are plotted against a variety of DD limits in Fig. 1.15. An axial-vector/vector mediator corresponds to a DM-nucleus cross section that does/does not depend on the spin of the nucleus, respectively known as the spin-dependent/spin-independent (SD/SI) cross section.

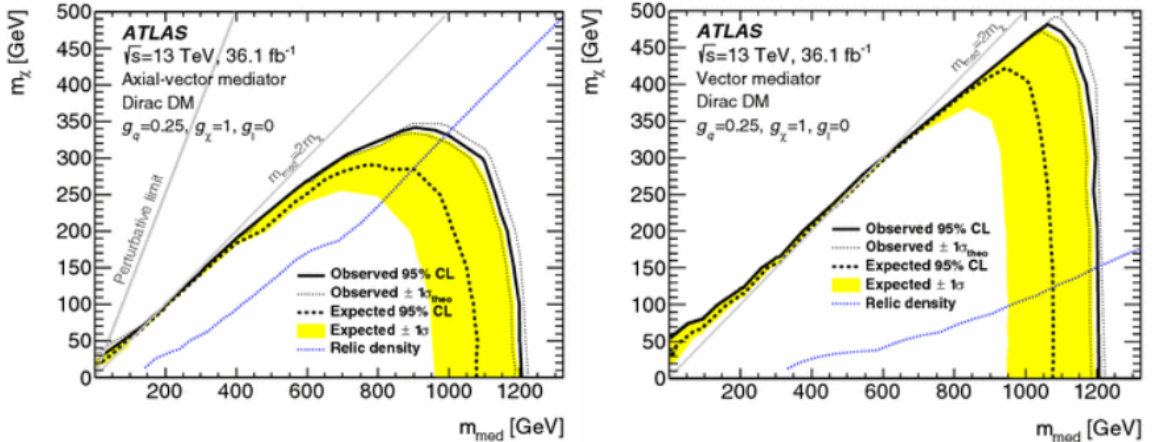


Figure 1.13: Limits on DM simplified model parameters set by the ATLAS experiment, as shown in [53]. Simplified models are excluded at 95% CL or above for parameter values under the contours. The relic density curves correspond to constraints on the cosmological DM abundance set by Planck satellite measurements [28].

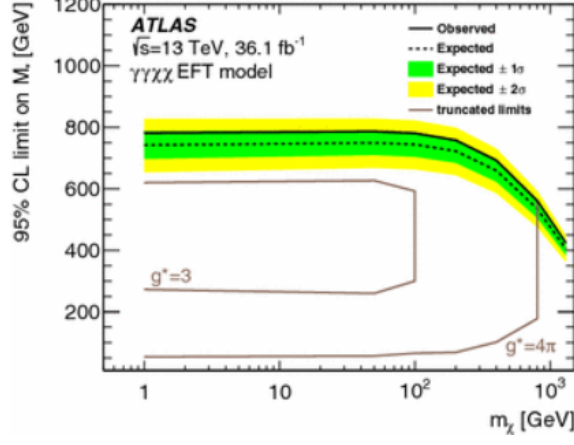


Figure 1.14: Limits on the DM-EWK EFT set by the ATLAS experiment, as shown in [53]. The DM-EWK EFT is excluded at 95% CL or above for values of  $\Lambda$  under the contour.

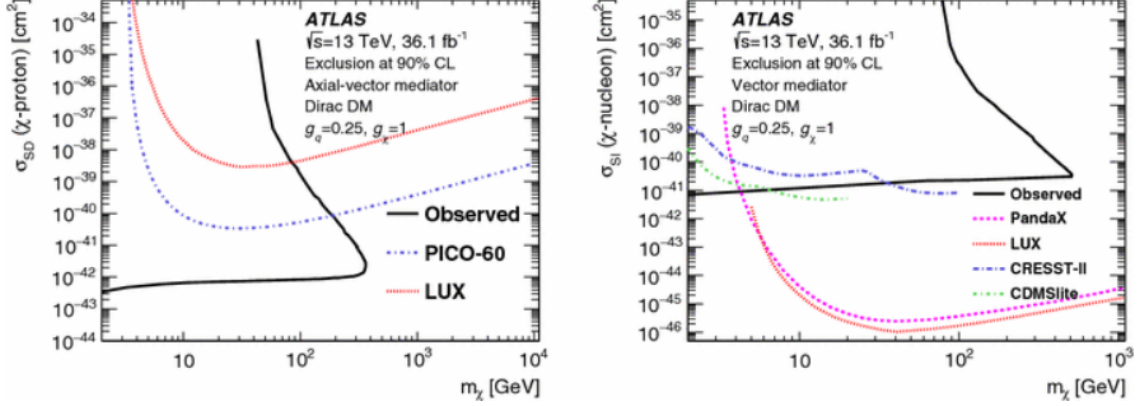


Figure 1.15: Limits on low-energy DM-nucleon scattering cross sections set by the ATLAS experiment, as shown in [53]. The ATLAS limits are compared against limits on the SD cross section from PICO-60 [54] and LUX [55] (left) and limits on the SI cross section from PandaX-II [56], LUX [57], CRESST-II [58], and CDMSlite [59] (right). Scattering cross sections are excluded at 90% CL or more above the contours.

All of the preceding limits were derived for  $g_{\text{DM}} = 1$  and  $g_q = 0.25$ , which matches the couplings used for the results obtained herein. By convention, this is the most commonly investigated set of values for these couplings, but studies have been done

using alternative values, some of which include a small nonzero coupling between the new mediator and charged leptons (e.g. [53]).

None of these analyses report any significant evidence of BSM physics.

## 1.6 ADD gravitons

We finally examine a model of gravitation in extra dimensions originally proposed by Arkani-Hamed, Dimopoulos, and Dvali (ADD) [60]. Gravity typically affects SM particles much, much less than the other fundamental interactions. The weakness of gravity is often expressed in terms of a fundamental mass scale  $M_{\text{Pl}}$  ( $\sim 10^{19}$  GeV), which is many orders of magnitude larger than the masses of the EWK bosons ( $\sim 10^2$  GeV). Particle-level gravitational interactions are correspondingly sharply suppressed. The proposed boson of gravitation, the graviton, has yet to be detected and is not part of the SM. The mystery of why  $M_{\text{Pl}}$  is so much larger than the EWK mass scale has been called the “Hierarchy problem,” and the desire for a more elegant formulation has been a productive stimulus for BSM theories [60, 61].

Everyday experience indicates that there are 3 dimensions of space and 1 dimension of time, and the SM assumes this to be true. The ADD model begins with the observation that, if there are  $n$  extra spatial dimensions beyond the usual 3, we might not be able to directly perceive them if all the SM particles are confined by some as-yet-unspecified mechanism to a 3+1-dimensional subspace (the “brane”) of the full  $n+3+1$ -dimensional spacetime (the “bulk”). In contrast, gravitons in this model are able to propagate freely throughout the bulk.

Gravitation in the bulk is characterized by its own mass scale  $M_{\text{D}}$  distinct from the mass scale  $M_{\text{Pl}}$  that characterizes gravitation as perceived by particles confined to the brane. If the extra dimensions are not extended infinitely like the dimensions of

common experience, but rather “compactified” into a finite volume of characteristic radius  $R$ , then for a sufficiently mild energy density in the vicinity of the brane,  $M_{\text{Pl}}^2 \approx M_{\text{D}}^{n+2} R^n$  [60, 62]. For a modest number of extra dimensions (e.g.  $3 \leq n \leq 6$ ), the observed large value of  $M_{\text{Pl}}$  could then really be a consequence of a large value for  $R$ , while the gravitational scale  $M_{\text{D}}$  could be closer to or even fundamentally the same thing as the EWK scale. In light of this possibility, ADD model predictions are typically examined for values of  $M_{\text{D}}$  in the vicinity of 1 TeV.

The cross sections for a variety of graviton production scenarios are calculated in ref. [62], using a low-energy EFT approximation of GR in which  $M_{\text{D}}$  serves as the suppression scale. At higher energies the specific details of the geometry of the extra dimensions, and phenomena uniquely predicted by a full quantum theory of gravitation, would start to become apparent. These are both unknown, so the EFT is appropriately silent on the outcome of scattering events with energies above  $M_{\text{D}}$ .

The ratio  $M_{\text{Pl}}/M_{\text{D}}$  essentially expresses the wide range of kinematic possibilities that open up for gravitons with the addition of extra dimensions. After summing over all of these possibilities, the resulting cross section is high enough for graviton production to be probed with existing collider experiments. Gravitons couple to every SM particle, although the coupling is still sufficiently weak that an emitted graviton will generally not interact with a detector element. This results in a monophoton signature if it is emitted opposite a photon, as illustrated in Fig. 1.16.

### 1.6.1 Previous searches

For distances  $r$  much larger than  $R$ , the effective gravitational potential has the  $1/r$  form proposed by Isaac Newton. However, for  $r \ll R$ , the Newton’s law potential is multiplied by  $(R/r)^n$ , leading to significant deviations from Newtonian gravitational behavior. If  $M_{\text{D}} \approx 1$  TeV and  $n = 1$ , then to reproduce the observed value of  $M_{\text{Pl}}$ ,



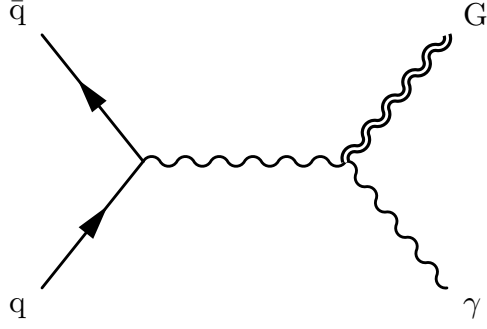


Figure 1.16: Diagram illustrating ADD graviton emission resulting in a monophoton signature.

$R$  must be  $\sim 10^{13}$  cm, which would result in noticeable differences in the orbits of the planets [60]. The case  $n = 2$  is disfavored by precision measurements of Newton's law over distances on the order of 0.1 mm [61].

As in the case of the aTGC model, collider limits become strictly more stringent with increases in collider energy, starting from the LEP and moving up through the Tevatron to the LHC. Representative curves from each of these are shown in Fig. 1.17, which also shows that collider limits on  $M_D$  dominate noncollider limits for  $n \geq 3$ .

Prior to the present analysis, the most stringent limits in the monophoton final state were set in the last published results from CMS, based on  $12.9 \text{ fb}^{-1}$  of data collected in the first half of 2016 [52]. The ADD model was excluded at 95% CL for  $M_D$  up to 2.31 TeV for  $n = 3$ , climbing to 2.49 TeV at  $n = 6$ , as shown in Fig. 1.18.

None of these analyses report any significant evidence of BSM physics.

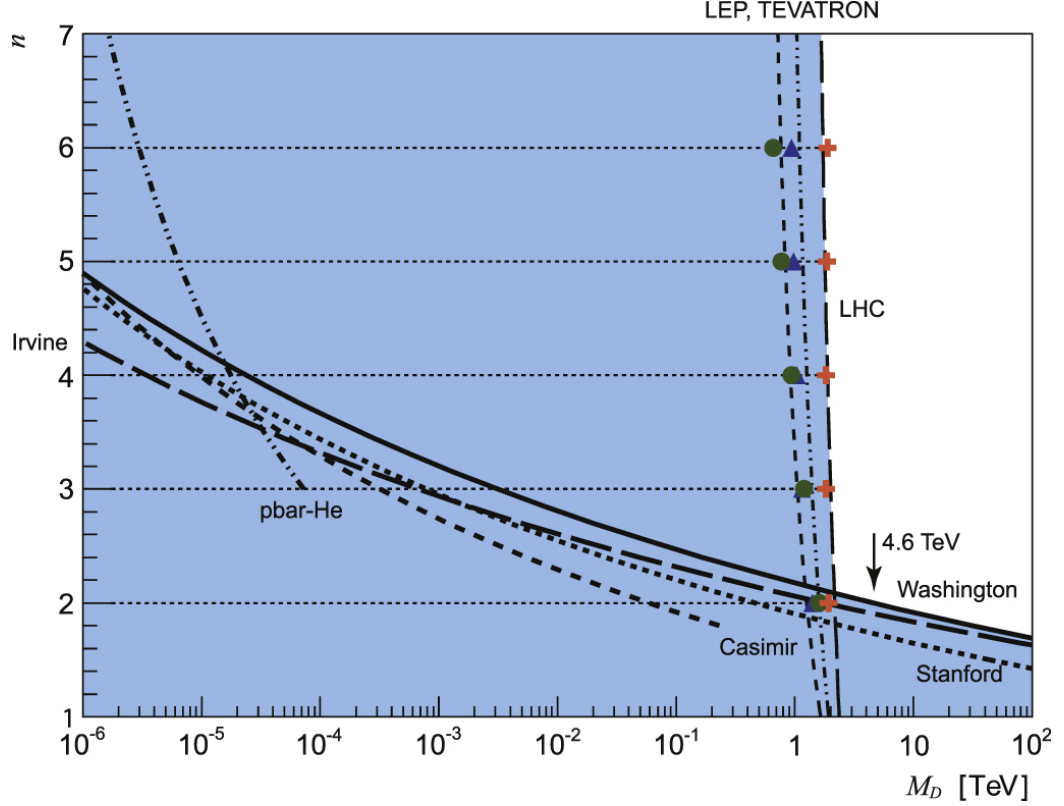


Figure 1.17: Comparison of collider and noncollider limits on ADD model parameters, as shown in [61]. The marked points are monojet limits from the LEP [63], Tevatron [64], and LHC [61,65,66]. The Irvine [67,68], Washington [69], and Stanford [70] curves come from direct measurements of Newton’s law. The Casimir curve [61] synthesizes of a range of experimental results that constrain the existence of strong gravity using the Casimir force, and the pbar-HE curve [61, 71] comes from analyses of electron double scattering and exotic atom spectroscopy. The ADD model is excluded at 95% CL or more in the shaded region.

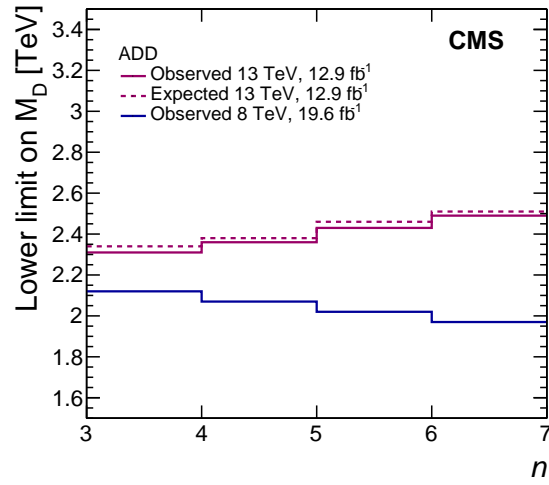


Figure 1.18: ADD limits set by the CMS experiment using data from the first half of 2016, as shown in [52]. Limits from the previous CMS analysis of 8 TeV data [46] are also shown. The ADD model for a given  $n$  (specified by the left edge of each bin) is excluded at 95% CL or more for  $M_D$  below the curves.

## Chapter 2

# The CMS experiment and the LHC

## 2.1 The LHC

The Large Hadron Collider (LHC) [72] at CERN is, as the name suggests, the world's largest and most powerful particle accelerator, used to collide protons as well as heavy ions. Experiments attached to the collider examine the collision debris, from which features of the parent hard-scattering process may be inferred, allowing models such as those described in Chap. 1 to be tested.

The collider consists of a roughly octagonal tunnel 26.7 km in circumference, along with its RF cavities 2.1.1, magnets 2.1.2, and cryogenic and vacuum systems. The tunnel lies between 45 and 170 m underground, straddling the French–Swiss border near Geneva, Switzerland, and accessible via shafts to the surface dug at 8 points around the perimeter of the octagon, one for each 8,528 m-long straight section. The four main LHC experiments surround the LHC beam pipe at four of these points: ATLAS [73] at point 1, ALICE [74] at point 2, CMS [75] at point 5, and LHCb [76] at point 8.

The 8 straight sections are joined by a corresponding number of arc sections, each

of which has a radius of curvature  $R = 2.804$  km. This radius constrains the kinetic energy of a relativistic proton bent in a circular trajectory by a magnetic field of magnitude  $B$ , via the relation

$$E = eBRc \quad (2.1)$$

where  $e$  is the electric charge of a proton and  $c$  is the speed of light. Accordingly, higher-energy colliders tend to be built with larger circumferences than lower-energy colliders.

Smaller accelerators including the Proton Synchrotron (PS) and Super Proton Synchrotron (SPS) used to be flagship accelerators in their own right, but now chiefly serve as intermediate stages in an accelerator complex that feeds the LHC. The LHC itself occupies the tunnel originally dug to house the Large Electron-Positron (LEP) collider [77], which collided electrons and their antipartners (positrons) and ran from 1989 until 2000, setting some of the original results listed in Chap. 1. The Tevatron [78], which ran from 1983 to 2011, occupied a smaller tunnel but achieved higher energies than LEP by accelerating heavier particles: protons and their antipartners. The LHC, inaugurated in 2008, accelerates protons in the world’s largest accelerator tunnel, with state-of-the-art bending magnets 2.1.2, allowing it to achieve unprecedented particle collision energies.

### 2.1.1 Proton acceleration

Protons are accelerated in stages beginning with the LINAC2, which receives ionized hydrogen gas and accelerates it to 50 MeV before sending it to the PS booster, which brings them up to 1.4 GeV. The protons are then sent to the PS, taking them to 25 GeV, and after that to the SPS, which pushes them to 450 GeV before finally injecting two counter-rotating beams into the LHC. These beams can be made to collide at 4 points around the ring, corresponding to each of the four main experiments.

A proton may be accelerated by passing through a radio-frequency (RF) cavity, which generates an oscillating electromagnetic field. Forward acceleration only results if the proton passes through the RF cavity at an opportune point in its oscillation cycle. Thus, rather than circulating in a continuous beam, protons are segregated into discrete “bunches.” In the LHC, the RF frequency is tuned to 400.790 MHz, and bunches are spaced so as to keep 10 RF oscillations between each bunch. This corresponds to a minimum bunch separation of 24.95 ns in time, with enough length in the tunnel to fit exactly 3564 bunches, orbiting with a frequency  $f_{\text{rev}} = 11.245$  kHz. A maximum of 2808 bunches can be injected in practice, to allow a sufficiently long empty interval for the beam injection and beam dump redirector magnets to activate; other operational constraints can reduce this further. In 2016, the typical number of bunches per beam  $n_b$  was 2076.

Each bunch contains many billions of protons: in 2016, the typical number of protons per bunch  $N_b$  was  $1.25 \times 10^{11}$ , higher than the original LHC design value of  $1.15 \times 10^{11}$ . Various parameters describing the geometric arrangement of the bunches are listed in Table ?? . These determine the instantaneous luminosity  $\mathcal{L}$  at the collision points, via

$$\mathcal{L} = \frac{N_b^2 n_b f_{\text{rev}} \gamma_r}{4\pi \epsilon_n \beta^*} \left( 1 + \frac{\theta_c^2 \sigma_z^2 \gamma_r}{4\epsilon_n \beta^*} \right)^{-1/2} \quad (2.2)$$

in which the relativistic factor  $\gamma_r = E_{\text{beam}}/m_p$  has a value of 6930 for  $E_{\text{beam}} = 6.5$  TeV. The value of  $\mathcal{L}$  corresponding to the typical 2016 parameter values listed above is  $1.3 \times 10^{34} \text{ cm}^{-2}\text{s}^{-1}$ .

### 2.1.2 Magnets and beam halo

Beam halo is an important component of the monophoton analysis and it comes from here.

## **2.2 The CMS experiment**

### **2.2.1 Coordinate system**

### **2.2.2 Superconducting solenoid and silicon tracking system**

### **2.2.3 Electromagnetic calorimeter**

The discussion of APDs segues into an introduction to ECAL spikes.

### **2.2.4 Hadronic calorimeter**

### **2.2.5 Muon systems**

### **2.2.6 Trigger system**

### **2.2.7 Luminosity measurement**

# Chapter 3

## Simulation

3.1 Hard process generation

3.2 Parton distribution functions

3.3 Parton showering and hadronization

3.4 Pileup simulation

3.5 Detector simulation



## Chapter 4

# Object reconstruction and selection

### 4.1 The particle-flow algorithm

### 4.2 Photons and electrons

### 4.3 Muons

### 4.4 Jets and missing transverse momentum

A discussion of jets is followed by a definition of  $p_T^{\text{miss}}$  and Type-1  $p_T^{\text{miss}}$  corrections.

### 4.5 Primary vertex

# Chapter 5

## Event selection

### 5.1 The monophoton signature and background sources

Summarize how each of the physics processes being analyzed exhibits a monophoton signature. List the sources of background in the monophoton channel, to justify the ensuing cuts.

### 5.2 Trigger and $p_T^{\text{miss}}$ filters

Trigger path, trigger efficiency

$p_T^{\text{miss}}$  filters

### 5.3 Photon

Photon kinematic cuts; Photon ID definition, efficiency; Spike and beam halo cuts; phoET-dependent cross section corrections

## 5.4 Missing transverse momentum

$$p_{\text{T}}^{\text{miss}} > 170 \text{ GeV}; \Delta\phi(\gamma, \vec{p}_{\text{T}}^{\text{miss}}) > 0.5; \min\Delta\phi(\text{jets}, \vec{p}_{\text{T}}^{\text{miss}}) > 0.5; E_{\text{T}}^{\gamma}/p_{\text{T}}^{\text{miss}} < 1.4$$

## 5.5 Lepton vetoes

Electron selection; Muon selection

## 5.6 Single electron control region

## 5.7 Single muon control region

## 5.8 Dielectron control region

## 5.9 Dimuon control region

# Chapter 6

## Background estimation

For each component, describe its estimation and uncertainties

### 6.1 Simulated backgrounds

### 6.2 Electron faking photon

### 6.3 Jet faking photon

### 6.4 Spikes

### 6.5 Beam halo

### 6.6 Transfer factors

### 6.7 Likelihood function

# Chapter 7

## Results

### 7.1 $Z(\nu\bar{\nu})\gamma$ cross section

### 7.2 aTGC limits

### 7.3 DM simplified model limits

### 7.4 ADD limits

## Chapter 8

## Conclusions

### 8.1 Summary

### 8.2 Outlook

# Bibliography

- [1] F. Halzen and A. Martin, *Quarks & Leptons: An introductory course in modern particle physics*. John Wiley & Sons, 1984.
- [2] V. Barger and R. Phillips, *Collider Physics*. Westview Press, 1996.
- [3] M. Peskin and D. Schroeder, *An Introduction to Quantum Field Theory*. Westview Press, 1995.
- [4] M. Srednicki, *Quantum Field Theory*. Cambridge University Press, 2007.
- [5] M. Schwartz, *Quantum Field Theory and the Standard Model*. Cambridge University Press, 2013.
- [6] M. Tanabashi *et al.*, “The Review of Particle Physics,” *Phys. Rev. D* **98** (2018) 030001, doi:10.1103/PhysRevD.98.030001.
- [7] A. Denner, S. Dittmaier, M. Hecht, and C. Pasold, “NLO QCD and electroweak corrections to  $W + \gamma$  production with leptonic  $W$ -boson decays,” *JHEP* **2015** (2015) arXiv:1412.7421, doi:10.1007/JHEP04(2015)018.
- [8] A. Denner, S. Dittmaier, M. Hecht, and C. Pasold, “NLO QCD and electroweak corrections to  $Z + \gamma$  production with leptonic  $Z$ -boson decays,” *JHEP* **2016** (2016) arXiv:1510.08742, doi:10.1007/JHEP02(2016)187.
- [9] M. Grazzini, S. Kallweit, D. Rathlev, and A. Torre, “ $Z\gamma$  production at hadron colliders in NNLO QCD,” *Phys. Lett. B* **731** (2014) 204, arXiv:1309.7000, doi:10.1016/j.physletb.2014.02.037.
- [10] M. Grazzini, S. Kallweit, and D. Rathlev, “ $W\gamma$  and  $Z\gamma$  production at the LHC in NNLO QCD,” *JHEP* **2015** (2015) 85, arXiv:1504.01330, doi:10.1007/JHEP07(2015)085.

- [11] L3 Collaboration, “Study of the  $e^+e^- \rightarrow Z\gamma$  process at LEP and limits on triple neutral-gauge-boson couplings,” *Phys. Lett. B* **597** (2004) 119, doi:10.1016/j.physletb.2004.07.002.
- [12] V. Abazov *et al.*, “Measurement of the  $Z\gamma \rightarrow \nu\bar{\nu}\gamma$  Production Cross Section and Limits on Anomalous  $ZZ\gamma$  and  $Z\gamma\gamma$  Couplings in  $p\bar{p}$  Collisions at  $\sqrt{s} = 1.96$  TeV,” *Phys. Rev. Lett.* **102** (2009) 201802, doi:10.1103/PhysRevLett.102.201802.
- [13] V. Khachatryan *et al.*, “Measurement of the  $Z\gamma \rightarrow \nu\bar{\nu}\gamma$  production cross section in  $pp$  collisions at  $\sqrt{s} = 8$  TeV and limits on anomalous  $ZZ\gamma$  and  $Z\gamma\gamma$  trilinear gauge boson couplings,” *Phys. Lett. B* **760** (2016) 448, arXiv:1602.07152, doi:10.1016/j.physletb.2016.06.080.
- [14] M. Grazzini, S. Kallweit, and M. Wiesemann, “Fully differential NNLO computations with MATRIX,” *EPJ C* **78** (2018) 537, arXiv:1711.06631, doi:10.1140/epjc/s10052-018-5771-7.
- [15] M. Aaboud *et al.*, “Measurement of the  $Z\gamma \rightarrow \nu\bar{\nu}\gamma$  production cross section in  $pp$  Collisions at  $\sqrt{s} = 13$  TeV with the ATLAS detector and limits on anomalous triple gauge-boson couplings.” 2018.
- [16] T. Gleisberg *et al.*, “Event generation with SHERPA 1.1,” *JHEP* **2009** (2009) 007, arXiv:0811.4622, doi:10.1088/1126-6708/2009/02/007.
- [17] J. Campbell, R. Ellis, and C. Williams, “Vector boson pair production at the LHC,” *JHEP* **2011** (2011) 18, arXiv:1105.0020, doi:10.1007/JHEP07(2011)018.
- [18] K. Hagiwara, R. Peccei, D. Zeppenfeld, and K. Hikasa, “Probing the weak boson sector in  $e^+e^- \rightarrow W^+W^-$ ,” *Nucl. Phys.* **282** (1987) 253, doi:10.1016/0550-3213(87)90685-7.
- [19] U. Baur and E. Berger, “Probing the weak boson sector in  $Z\gamma$  production at hadron colliders,” *Phys. Rev. D* **47** (1993) 4889, doi:10.1103/PhysRevD.47.4889.
- [20] U. Baur and D. Rainwater, “Probing neutral gauge boson self-interactions in  $ZZ$  production at hadron colliders,” *Phys. Rev. D* **62** (2000) 113011, arXiv:hep-ph/0008063, doi:10.1103/PhysRevD.62.113011.



- [21] S. Chatrchyan *et al.*, “Measurement of the  $W\gamma$  and  $Z\gamma$  inclusive cross sections in  $pp$  collisions at  $\sqrt{s} = 7$  TeV and limits on anomalous triple gauge boson couplings,” *Phys. Rev. D* **89** (2014) 092005, [arXiv:1308.6832](#), [doi:10.1103/PhysRevD.89.092005](#).
- [22] S. Chatrchyan *et al.*, “Measurement of the production cross section for  $Z\gamma \rightarrow \nu\bar{\nu}\gamma$  in  $pp$  collisions at  $\sqrt{s} = 7$  TeV and limits on  $ZZ\gamma$  and  $Z\gamma\gamma$  triple gauge boson couplings,” *JHEP* **10** (2013) 164, [arXiv:1309.1117](#), [doi:10.1007/JHEP10\(2013\)164](#).
- [23] D. Green, P. Meade, and M. Pleier, “Multiboson interactions at the LHC,” *Rev. Mod. Phys.* **89** (2017) 035008, [arXiv:1610.07572](#), [doi:10.1103/RevModPhys.89.035008](#).
- [24] The ALEPH Collaboration, The DELPHI collaboration, The L3 Collaboration, The OPAL Collaboration, and The LEP Electroweak Working Group, “Electroweak measurements in electron-positron collisions at W-boson-pair energies at LEP,” *Phys. Rep.* **532** (2013) 119, [arXiv:1302.3415](#), [doi:10.1016/j.physrep.2013.07.004](#).
- [25] T. Aaltonen *et al.*, “Limits on Anomalous Trilinear Gauge Couplings in  $Z\gamma$  Events from  $p\bar{p}$  Collisions at  $\sqrt{s} = 1.96$  TeV,” *Phys. Rev. Lett.* **107** (2011) 051802, [arXiv:1103.2990](#), [doi:10.1103/PhysRevLett.107.051802](#).
- [26] V. Abazov *et al.*, “ $Z\gamma$  production and limits on anomalous  $ZZ\gamma$  and  $Z\gamma\gamma$  couplings in  $p\bar{p}$  collisions at  $\sqrt{s} = 1.96$  TeV,” *Phys. Rev. D* **85** (2012) 052001, [arXiv:1111.3684](#), [doi:10.1103/PhysRevD.85.052001](#).
- [27] N. Ashby, “Relativity in the Global Positioning System,” *Living Rev. Relativ.* **6** (2003) 1, [doi:10.12942/lrr-2003-1](#).
- [28] N. Aghanim *et al.*, “Planck 2018 results. VI. Cosmological parameters,” [arXiv:1807.06209](#).
- [29] R. Wald, *General Relativity*. University of Chicago Press, 1984.
- [30] B. Abbott *et al.*, “Observation of Gravitational Waves from a Binary Black Hole Merger,” *Phys. Rev. Lett.* **116** (2016) 061102, [arXiv:1602.03837](#), [doi:10.1103/PhysRevLett.116.061102](#).

- [31] B. Abbott *et al.*, “Tests of general relativity with GW150914,” *Phys. Rev. Lett.* **116** (2016) 221101, [arXiv:1602.03841](#),  
[doi:10.1103/PhysRevLett.116.221101](#).
- [32] P. van Dokkum *et al.*, “A galaxy lacking dark matter,” *Nature* **555** (2018) 629,  
[arXiv:1803.10237](#), [doi:10.1038/nature25767](#).
- [33] M. Bartelmann and M. Maturi, “Weak gravitational lensing,”  
[arXiv:1612.06535](#).
- [34] P. Natarajan *et al.*, “Mapping substructure in the HST Frontier Fields cluster lenses and in cosmological simulations,” *Monthly Notices of the Royal Astronomical Society* **468** (2017) 1962, [arXiv:1702.04348](#),  
[doi:10.1093/mnras/stw3385](#).
- [35] S. Allen, A. Evrard, and A. Mantz, “Cosmological Parameters from Observations of Galaxy Clusters,” *ARAAS* **49** (2011) 409, [arXiv:1103.4829](#),  
[doi:10.1146/annurev-astro-081710-102514](#).
- [36] V. Springel *et al.*, “Simulating the joint evolution of quasars, galaxies and their large-scale distribution,” *Nature* **435** (2005) 629, [arXiv:astro-ph/0504097](#),  
[doi:10.1038/nature03597](#).
- [37] D. Clowe *et al.*, “A direct empirical proof of the existence of dark matter,” *Astrophys. J.* **648** (2006) L109, [arXiv:astro-ph/0608407](#),  
[doi:10.1086/508162](#).
- [38] J. de Swart, G. Bertone, and J. van Dongen, “How dark matter came to matter,” *Nature Astr.* **1** (2017) 0059, [arXiv:1703.00013](#),  
[doi:10.1038/s41550-017-0059](#).
- [39] G. Bertone, D. Hooper, and J. Silk, “Particle dark matter: evidence, candidates and constraints,” *Phys. Rep.* **405** (2005) 279,  
[arXiv:hep-ph/0404175](#), [doi:10.1016/j.physrep.2004.08.031](#).
- [40] R. Gaitskell, “Direct Detection of Dark Matter,” *Annu. Rev. Nucl. Part. Sci.* **54** (2004) 315, [doi:10.1146/annurev.nucl.54.070103.181244](#).
- [41] L. Baudis, “The Search for Dark Matter,” *Eur. Rev.* **26** (2018) 70,  
[arXiv:1801.08128](#), [doi:10.1017/S1062798717000783](#).

- [42] A. Nelson *et al.*, “Confronting the Fermi Line with LHC data: an Effective Theory of Dark Matter Interaction with Photons,” *Phys. Rev. D* **89** (2014) 056011, [arXiv:1307.5064](#), [doi:10.1103/PhysRevD.89.056011](#).
- [43] C. Degrande *et al.*, “Effective field theory: A modern approach to anomalous couplings,” *Annals of Phys.* **335** (2013) 21, [arXiv:1205.4231](#), [doi:10.1016/j.aop.2013.04.016](#).
- [44] D. Abercrombie *et al.*, “Dark Matter Benchmark Models for Early LHC Run-2 Searches: Report of the ATLAS/CMS Dark Matter Forum,” [arXiv:1507.00966](#).
- [45] G. Busoni *et al.*, “Recommendations on presenting LHC searches for missing transverse energy signals using simplified  $s$ -channel models of dark matter,” [arXiv:1603.04156](#).
- [46] “Search for new phenomena in monophoton final states in proton-proton collisions at  $\sqrt{s} = 8$  TeV,” *Phys. Lett. B* **755** (2016) 102, [arXiv:1410.8812](#), [doi:10.1016/j.physletb.2016.01.057](#).
- [47] “Search for new phenomena in events with a photon and missing transverse momentum in  $pp$  collisions at  $\sqrt{s} = 8$  TeV with the ATLAS detector,” *Phys. Rev. D* **91** (2015) 012008, [arXiv:1411.1559](#), [doi:10.1103/PhysRevD.91.012008](#).
- [48] Albert, A. on behalf of the CMS Collaboration, “Searches for dark matter with CMS.” ICHEP 2018, 2018.
- [49] A. Sirunyan *et al.*, “Search for new physics in events with a leptonically decaying  $Z$  boson and a large transverse momentum imbalance in proton-proton collisions at  $\sqrt{s} = 13$  TeV,” *Eur. Phys. J. C* **78** (2018) 291, [arXiv:1711.00431](#), [doi:10.1140/epjc/s10052-018-5740-1](#).
- [50] A. Sirunyan *et al.*, “Search for new physics in final states with an energetic jet or a hadronically decaying  $W$  or  $Z$  boson and transverse momentum imbalance at  $\sqrt{s} = 13$  TeV,” *Phys. Rev. D* **97** (2018) 092005, [arXiv:1712.02345](#), [doi:10.1103/PhysRevD.97.092005](#).

- [51] A. Sirunyan *et al.*, “Search for new physics in final states with a single photon and missing transverse momentum in proton-proton collisions at  $\sqrt{s} = 13$  TeV,” [arXiv:1810.00196](#).
- [52] A. Sirunyan *et al.*, “Search for new physics in the monophoton final state in proton-proton collisions at  $\sqrt{s} = 13$  TeV,” *JHEP* **2017** (2017) 73, [arXiv:1706.03794](#), [doi:10.1007/JHEP10\(2017\)073](#).
- [53] M. Aaboud *et al.*, “Search for dark matter at  $\sqrt{s} = 13$  TeV in final states containing an energetic photon and large missing transverse momentum with the ATLAS detector,” *Eur. Phys. J. C* **77** (2017) 393, [arXiv:1704.03848](#), [doi:10.1140/epjc/s10052-017-4965-8](#).
- [54] C. Amole *et al.*, “Dark Matter Search Results from the PICO-60 C<sub>3</sub>F<sub>8</sub> Bubble Chamber,” *Phys. Rev. Lett.* **118** (2017) 251301, [arXiv:1702.07666](#), [doi:10.1103/PhysRevLett.118.251301](#).
- [55] D. Akerib *et al.*, “Results on the Spin-Dependent Scattering of Weakly Interacting Massive Particles on Nucleons from the Run 3 Data of the LUX Experiment,” *Phys. Rev. Lett.* **116** (2016) 161302, [arXiv:1602.03489](#), [doi:10.1103/PhysRevLett.116.161302](#).
- [56] A. Tan *et al.*, “Dark Matter Results from First 98.7 Days of Data from the PandaX-II Experiment,” *Phys. Rev. Lett.* **117** (2016) 121303, [arXiv:1607.07400](#), [doi:10.1103/PhysRevLett.117.121303](#).
- [57] D. Akerib *et al.*, “Results from a search for dark matter in the complete LUX exposure,” *Phys. Rev. Lett.* **118** (2017) 021303, [arXiv:1608.07648](#), [doi:10.1103/PhysRevLett.118.021303](#).
- [58] G. Angloher *et al.*, “Results on light dark matter particles with a low-threshold CRESST-II detector,” *Eur. Phys. J. C* **76** (2016) 25, [arXiv:1509.01515](#), [doi:10.1140/epjc/s10052-016-3877-3](#).
- [59] R. Agnese *et al.*, “New Results from the Search for Low-Mass Weakly Interacting Massive Particles with the CDMS Low Ionization Threshold Experiment,” *Phys. Rev. Lett.* **116** (2016) 071301, [arXiv:1509.02448](#), [doi:10.1103/PhysRevLett.116.071301](#).

- [60] N. Arkani-Hamed, S. Dimopoulos, and G. Dvali, “The hierarchy problem and new dimensions at a millimeter,” *Phys. Lett. B* **429** (1998) 263, [arXiv:hep-ph/9803315](#), [doi:10.1016/S0370-2693\(98\)00466-3](#).
- [61] J. Murata and S. Tanaka, “A review of short-range gravity experiments in the LHC era,” *Class. Quant. Grav.* **32** (2015) 033001, [arXiv:1408.3588](#), [doi:10.1088/0264-9381/32/3/033001](#).
- [62] G. Giudice, R. Rattazzi, and J. Wells, “Quantum gravity and extra dimensions at high-energy colliders,” *Nucl. Phys. B* **544** (1999) 3, [arXiv:hep-ph/9811291](#), [doi:10.1016/S0550-3213\(99\)00044-9](#).
- [63] S. Ask, “Search For Extra Dimensions At LEP,” *Proceedings of the 32nd International Conference on High-Energy Physics* (2005) 1289, [arXiv:hep-ex/0410004](#), [doi:10.1142/9789812702227\\_0266](#).
- [64] T. Aaltonen *et al.*, “Search for Large Extra Dimensions in Final States Containing One Photon or Jet and Large Missing Transverse Energy Produced in  $p\bar{p}$  Collisions at  $\sqrt{s} = 1.96$  TeV,” *Phys. Rev. Lett.* **101** (2008) 181602, [arXiv:0807.3132](#), [doi:10.1103/PhysRevLett.101.181602](#).
- [65] G. Aad *et al.*, “Search for new phenomena with the monojet and missing transverse momentum signature using the ATLAS detector in  $\sqrt{s} = 7$  TeV proton-proton collisions,” *Phys. Lett. B* **705** (2011) 294, [arXiv:1106.5327](#), [doi:10.1016/j.physletb.2011.10.006](#).
- [66] G. Aad *et al.*, “Search for dark matter candidates and large extra dimensions in events with a photon and missing transverse momentum in  $pp$  collision data at  $\sqrt{s} = 7$  TeV with the ATLAS detector,” *Phys. Rev. Lett.* **110** (2013) 011802, [arXiv:1209.4625](#), [doi:10.1103/PhysRevLett.110.011802](#).
- [67] J. Hoskins *et al.*, “Experimental tests of the gravitational inverse-square law for mass separations from 2 to 105 cm,” *Phys. Rev. D* **32** (1985) 3084, [doi:10.1103/PhysRevD.32.3084](#).
- [68] R. Spero *et al.*, “Test of the Gravitational Inverse-Square Law at Laboratory Distances,” *Phys. Rev. Lett.* **44** (1980) 1645, [doi:10.1103/PhysRevLett.44.1645](#).

- [69] D. Kapner *et al.*, “Tests of the Gravitational Inverse-Square Law below the Dark-Energy Length Scale,” *Phys. rev. Lett.* **98** (2007) 021101, [arXiv:hep-ph/0611184](#), [doi:10.1103/PhysRevLett.98.021101](#).
- [70] A. Geraci *et al.*, “Improved constraints on non-Newtonian forces at 10 microns,” *Phys. Rev. D* **78** (2008) 022002, [arXiv:0802.2350](#), [doi:10.1103/PhysRevD.78.022002](#).
- [71] S. Tanaka *et al.*, “Search of non-standard strong gravity at nuclear scale using electron spin geodetic precession,” *EPJ Web of Conferences* **66** (2014) 05021, [doi:10.1051/epjconf/20146605021](#).
- [72] L. Evans and P. Bryant, “LHC Machine,” *JINST* **3** (2008) S08001, [doi:10.1088/1748-0221/3/08/S08001](#).
- [73] G. Aad *et al.*, “The ATLAS Experiment at the CERN Large Hadron Collider,” *JINST* **3** (2008) S08003, [doi:10.1088/1748-0221/3/08/S08003](#).
- [74] K. Aamodt *et al.*, “The ALICE experiment at the CERN LHC,” *JINST* **3** (2008) S08002, [doi:10.1088/1748-0221/3/08/S08002](#).
- [75] S. Chatrchyan *et al.*, “The CMS experiment at the CERN LHC,” *JINST* **3** (2008) S08004, [doi:10.1088/1748-0221/3/08/S08004](#).
- [76] A. Alves *et al.*, “The LHCb Detector at the LHC,” *JINST* **3** (2008) S08005, [doi:10.1088/1748-0221/3/08/S08005](#).
- [77] H. Schopper, *LEP - The Lord of the Collider Rings at CERN 1980-2000*. Springer-Verlag Berlin Heidelberg, 2009. [doi:10.1007/978-3-540-89301-1](#).
- [78] V. Lebedev and V. Shiltsev, *Accelerator Physics at the Tevatron Collider*. Springer-Verlag New York, 2014. [doi:10.1007/978-1-4939-0885-1](#).